

Study of Quasielastic Barrier Distributions as a Step towards the Synthesis of Superheavy Elements with Hot Fusion Reactions

T. Tanaka^{1,2,3}, K. Morita,^{1,2} K. Morimoto,¹ D. Kaji,¹ H. Haba,¹ R. A. Boll,⁴ N. T. Brewer⁴, S. Van Cleve,⁴ D. J. Dean,⁴ S. Ishizawa,^{1,5} Y. Ito,^{1,6} Y. Komori,¹ K. Nishio,⁶ T. Niwase,^{1,2} B. C. Rasco⁴, J. B. Roberto,⁴ K. P. Rykaczewski,⁴ H. Sakai¹, D. W. Stracener⁴ and K. Hagino^{7,8,9}

¹RIKEN Nishina Center for Accelerator-Based Science, Saitama 351-0198, Japan

²Department of Physics, Kyushu University, Fukuoka 819-0395, Japan

³Department of Nuclear Physics, Research School of Physics and Engineering, The Australian National University, Canberra, Australian Capital Territory 2601, Australia

⁴Oak Ridge National Laboratory, Oak Ridge, Tennessee 37831, USA

⁵Graduate School of Science and Engineering, Yamagata University, Yamagata 990-8560, Japan

⁶Advanced Science Research Center, Japan Atomic Energy Agency, Tokai, Ibaraki 319-1195, Japan

⁷Department of Physics, Tohoku University, Sendai 980-8578, Japan

⁸Research Center for Electron Photon Science, Tohoku University, Sendai 982-0826, Japan

⁹Department of Physics, Kyoto University, Kyoto 606-8502, Japan

(Received 6 October 2019; revised manuscript received 6 December 2019; accepted 9 January 2020; published 5 February 2020)

The excitation functions for quasielastic scattering of $^{22}\text{Ne} + ^{248}\text{Cm}$, $^{26}\text{Mg} + ^{248}\text{Cm}$, and $^{48}\text{Ca} + ^{238}\text{U}$ are measured using a gas-filled recoil ion separator. The quasielastic barrier distributions are extracted for these systems and are compared with coupled-channel calculations. The results indicate that the barrier distribution is affected dominantly by deformation of the actinide target nuclei, but also by vibrational or rotational excitations of the projectile nuclei, as well as neutron transfer processes before capture. From a comparison between the experimental barrier distributions and the evaporation residue cross sections for Sg ($Z = 106$), Hs (108), Cn (112), and Lv (116), it is suggested that the hot fusion reactions take advantage of a compact collision, where the projectile approaches along the short axis of a prolately deformed nucleus. A new method is proposed to estimate the optimum incident energy to synthesize unknown superheavy nuclei using the barrier distribution.

DOI: [10.1103/PhysRevLett.124.052502](https://doi.org/10.1103/PhysRevLett.124.052502)

Atomic nuclei are particularly stabilized when both neutrons and protons have magic numbers. Such nuclei are called doubly magic nuclei: ^4He , ^{16}O , ^{40}Ca , ^{48}Ca , and ^{208}Pb are the stable doubly magic isotopes. What will be the next doubly magic nucleus beyond ^{208}Pb ? Theoretical physicists have made several different predictions for the next proton magic number, such as $Z = 114$, 120, and 126 [1–5]. Nuclei located around the next doubly magic number are expected to have longer half-lives than the known superheavy nuclei (SHN), forming “the island of stability.” The long-lived SHN would also open a new type of chemistry study for the superheavy elements (SHE), which would necessitate a longer time to complete chemical procedures. The frontier of SHE, between Fl ($Z = 114$) and Og ($Z = 118$), has been synthesized by hot fusion reactions using a combination of the ^{48}Ca projectile with actinoid targets of Pu–Cf [6–10]. A possible signature of the evidence for the island of stability has been found in systematic studies of decay properties in the SHN region [10], even though the center of the island has not yet been reached.

A few research groups have attempted (or will attempt) to synthesize new elements, $Z = 119$ and 120, in order to

open the door to the new period (that is, the eighth period) in the periodic table, as well as to understand the stability around the closed-proton shells in the nuclear system [11–15]. In these experiments, projectile nuclei heavier than ^{48}Ca , such as ^{50}Ti , ^{51}V , and ^{54}Cr , are used, since Cf ($Z = 98$) is the heaviest element that is available with sufficient amounts to make a target material for evaporation residue (ER) measurements [14,16]. Cross sections of the reactions to produce these new elements are predicted to be much smaller than those for the existing elements [16–19]. These cross sections are known to be particularly sensitive to the incident energy. A new systematic study of the reaction dynamics with the heavier projectiles [16,20–22] is urged since the systematics with the ^{48}Ca projectile will not be sufficient to estimate the optimum way to synthesize the new elements, $Z = 119$ and 120 [16]. Reaction dynamics for the systems in which the ER cross sections are available should be systematically studied in order to extrapolate the optimal beam energy to produce these new SHE.

One of the most direct ways to understand the reaction mechanism and determine the optimum incident energy, at

which the evaporation residue cross section is maximized, will be provided by the capture barrier distribution [23–25]. In heavy-ion reactions, the Coulomb barrier is strongly modified by couplings of the relative motion between the colliding nuclei to several nuclear excitations [26,27] and deformation of the target nucleus [28,29], as well as nucleon transfer processes [30]. Such couplings lead to a distribution of the Coulomb barriers [26,31]. The barrier distribution can be obtained either from fusion reactions [31] or from quasielastic (QE) scattering [32], which is defined as the sum of all reaction processes other than capture (i.e., elastic scattering, inelastic scattering, and direct transfer channels). Many experimental studies have established the validity of the concept of the barrier distribution [26,33], and coupled-channel calculations have been successfully compared to the experimentally determined barrier distributions [30,34].

The barrier distribution refers to a barrier for a two-body system to reach the touching configuration. In medium-heavy mass systems, the compound nucleus is considered to be formed once the touching configuration is reached, as long as the pocket in the entrance channel potential exists. Therefore, the barrier distribution has customarily been referred to as the “fusion” barrier distribution. On the contrary, for the massive reactions, such as those that produce SHN, a substantial amount of the system cannot reach the compound nucleus due to the enhanced quasi-fission probability after overcoming the Coulomb barrier [35,36]. In that situation, it would be more appropriate to call it the “capture” barrier distribution.

In Ref. [25], the first result of a QE barrier distribution measurement using the gas-filled recoil ion separator (GARIS) [37,38] was reported. In the measurement, the QE cross sections for the angular momentum $l \sim 0$ were successfully obtained by measuring the target nuclei recoiling into the forward angle (which corresponds to $\theta_{\text{lab}} \sim 180^\circ$) [25]. This was in a marked contrast to the previous QE barrier distribution studies [23,24,32], which measured the recoiled projectilelike nuclei at backward angles ($\theta_{\text{lab}} \sim 170^\circ$ or smaller). An advantage to taking data at $l \sim 0$ is that one can make a direct comparison between a measured barrier distribution and experimental evaporation residue (ER) cross sections σ_{ER} without needing to map the data onto those at $l \sim 0$ using the effective energy [39]. Furthermore, this method greatly cleaned up background originating from other events, such as deep-inelastic (DI) collision, except for high-incident-energy points, since the cross sections of DI for projectilelike nuclei at backward angles are smaller than that of forward angles [40] and also because GARIS can utilize rigidity analysis of recoiled particles.

In this Letter, we apply the same method used in Ref. [25] to the $^{22}\text{Ne} + ^{248}\text{Cm}$, $^{26}\text{Mg} + ^{248}\text{Cm}$, and $^{48}\text{Ca} + ^{238}\text{U}$ reactions, relevant to hot fusion reactions for the production of SHN of Sg ($Z = 106$), Hs (108), and Cn (112), respectively, in order to carry out a systematic study

on the reaction dynamics for new SHE. For this purpose, we combine the results to that of our previous measurement for the $^{48}\text{Ca} + ^{248}\text{Cm}$ reaction to synthesize Lv ($Z = 116$) [25]. Whereas the previous study [25] discussed the difference in the optimum incident energy for cold ($^{48}\text{Ca} + ^{208}\text{Pb}$ and $^{50}\text{Ti} + ^{208}\text{Pb}$) and hot ($^{48}\text{Ca} + ^{248}\text{Cm}$) fusion reactions, in this Letter we use the systematic data to discuss mainly the fusion dynamics for hot fusion reactions toward a synthesis of the new SHN and SHE.

The experiments were performed at the RIKEN heavy-ion linear accelerator (RILAC) facility. Primary beams were prepared from an 18-GHz ECR ion source [41] feeding the RILAC [42] with $^{22}\text{Ne}^{6+}$, $^{26}\text{Mg}^{7+}$ ions, and with $^{48}\text{Ca}^{11+}$ using the micro-oven technique [43]. The beam energies were measured by two methods: magnetic rigidity measurement of the ions traversing a 90° bending magnet and a time-of-flight (TOF) measurement. The accuracy of the beam energy measurement system is 0.2%. The $^{248}\text{Cm}_2\text{O}_3$ ($^{238}\text{U}_3\text{O}_8$) targets were produced by electrodeposition of the material on 2.2- μm -thick (3.0- μm -thick) Ti backing foils [44], and the thickness was 490 $\mu\text{g}/\text{cm}^2$ (310 $\mu\text{g}/\text{cm}^2$). The recoiled targetlike particles were separated from the background by GARIS [37,38]. GARIS was mounted at 0° with respect to the beam line and had acceptance $\Delta\theta = \pm 68$ mrad and $\Delta\phi = \pm 57$ mrad. The magnetic rigidity of GARIS was typically set to 1.97 Tm for $^{22}\text{Ne} + ^{248}\text{Cm}$, 1.96 Tm for $^{26}\text{Mg} + ^{248}\text{Cm}$, and 1.68 Tm for $^{48}\text{Ca} + ^{238}\text{U}$. The focal plane detectors consisted of two TOF detectors, having 29.5-cm distance in between them, and a 16-strip position-sensitive silicon detector (PSD), placed behind. The PSD detector has an active area of 58×58 mm² and is transversely divided to 16 strips. Rutherford scattering events were measured using a silicon detector to normalize the cross sections. The detector has an active area of 3.6×3.6 mm² and was mounted either 25 or 142 cm downstream of the target at 45° with respect to the beam axis.

Figures 1(a) and 1(b) show a typical two-dimensional plot of the recorded events on the TOF versus energy for the reactions $^{48}\text{Ca} + ^{238}\text{U}$ at $E_{\text{c.m.}} = 165.1$ and 203.7 MeV, respectively. From the point of view of the kinematics calculations, the relation between the energy and TOF at a given particle mass ($m \propto E \times \text{TOF}^2$), and considering that tantalum is present in the beam path, the events in the plots were classified as ^{238}U targetlike events, ^{181}Ta sputtered out by impinging the beam on the beamstopper or the beam slits, and ^{48}Ca beamlike events.

Figure 1(c) shows the distribution of the ^{238}U targetlike nucleus over the PSD strips (No. 0–15) for reaction $^{48}\text{Ca} + ^{238}\text{U}$ at $E_{\text{c.m.}} = 165.1$ MeV. Strip 0 was located on the higher magnetic rigidity side, and strip 15 was on the opposite side. The strip distribution of strips 1–15 was used for the present analyses since strip 0 was out of order. The overall distribution of the targetlike nucleus slightly

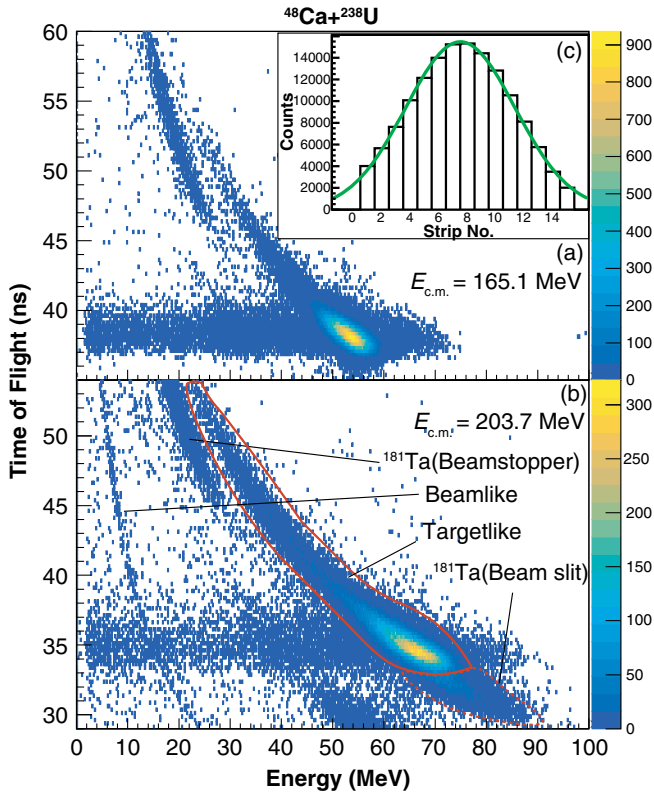


FIG. 1. Two-dimensional plots of the TOF versus the energy. The vertical axis shows the TOF measured by TOF detectors, and the horizontal axis shows the TOF detected by the PSD at (a) $E_{c.m.} = 165.1$ and (b) 203.7 MeV. (c) The strip distribution of targetlike events (black line boxes) with the Gaussian fit of the distribution (green line).

exceeds the PSD size. A Gaussian distribution (the green line) well reproduced the obtained distribution, which enabled us to estimate the total counts of targetlike events. The integral value of the Gaussian distribution was defined as the exact count for QE scattering events.

The measured excitation functions for the QE scattering cross section relative to the Rutherford cross section $d\sigma_{QE}/d\sigma_R$ (see Supplemental Material [45]) and the corresponding QE barrier distribution are indicated by the red or green symbols in Figs. 2 and 3. The barrier distributions were extracted using the point difference formula with two neighboring data points from the $d\sigma_{QE}/d\sigma_R$. The error bars account for the statistical and systematic uncertainties [46]. At the higher energy data points, indicated by the green symbols, DI events start to dominate over the QE events. This makes the clear selection of QE events difficult. These data points provide an upper limit for $d\sigma_{QE}/d\sigma_R$. See Ref. [46] for further details of the experiment.

The experimental results were interpreted by the coupled-channels approach on the basis of the computer code CCFULL [34,55], in which a Woods-Saxon potential is employed for an internuclear potential. The parameters of the real part of the potential, which were used in the present

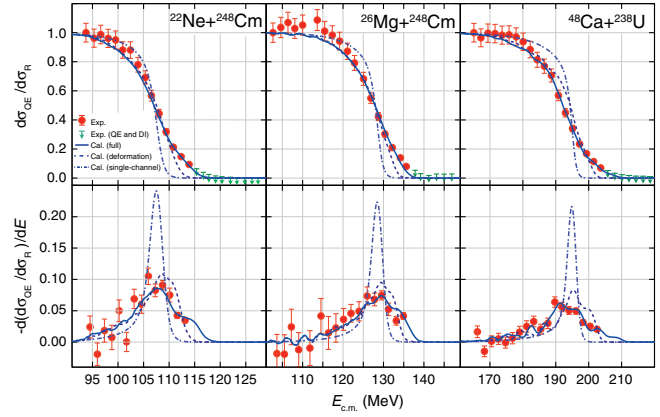


FIG. 2. The measured excitation functions for the QE scattering cross section relative to the Rutherford cross section (upper) and the corresponding QE barrier distribution (lower). The red and green symbols indicate the experimental data from this Letter. The curves denote the results of the coupled-channels calculation (see text).

analyses, were $r_0 = 1.18$ and $a_0 = 0.69$ fm, for the radius and the diffuseness parameters, respectively. Those of the imaginary part were $r_w = 1.0$ fm, $a_w = 0.4$ fm, and $V_w = 50$ MeV. The radius and diffuseness parameters of the real part of the potential for each system were close to those of the Akyüz-Winther potential [56]. Following the previous works [24,25], the depth parameter V_0 of the real part of the internuclear potential was adjusted to reproduce the measured excitation functions.

The dashed blue curves in Fig. 2 show the results with the deformation effect of the target nuclei. To this end, the deformation parameters of $\beta_2 = 0.2972$ [57], $\beta_4 = 0.039$ [58], and $\beta_6 = 0.030$ for ^{248}Cm , and $\beta_2 = 0.2860$ [57], $\beta_4 = 0.050$ [28], and $\beta_6 = 0.050$ for ^{238}U were employed. For a comparison, the figure also shows the results of the no-coupling case by the dot-dashed lines. From a comparison of these two results, one can clearly see that the barrier distributions are strongly influenced by the deformation effect of the target nuclei.

We then included the couplings to low-lying collective excitations in the projectile nuclei as well as a neutron transfer process before the capture using the orientation average formula [39] for the deformed targets. For the collective excitations, we considered the quadrupole phonon excitations in ^{22}Ne and ^{26}Mg at 1.27 MeV with $\beta_2 = 0.562$ and at 1.808 MeV and $\beta_2 = 0.487$, respectively [57], as well as the octupole phonon excitation in ^{48}Ca at 4.507 MeV with $\beta_3 = 0.1748$ [59]. The transfer Q values were taken to be those for the ground state to the ground state transitions, $Q_{gg} = -1.01$ MeV for the reaction of $^{22}\text{Ne} + ^{248}\text{Cm}$, 0.23 MeV for $^{26}\text{Mg} + ^{248}\text{Cm}$, -1.00 MeV for $^{48}\text{Ca} + ^{238}\text{U}$, and -1.06 MeV for $^{48}\text{Ca} + ^{248}\text{Cm}$, which were estimated based on a mass table in Ref. [58]. The coupling strengths to the transfer channels of $F_{tr} = 0.30$ for

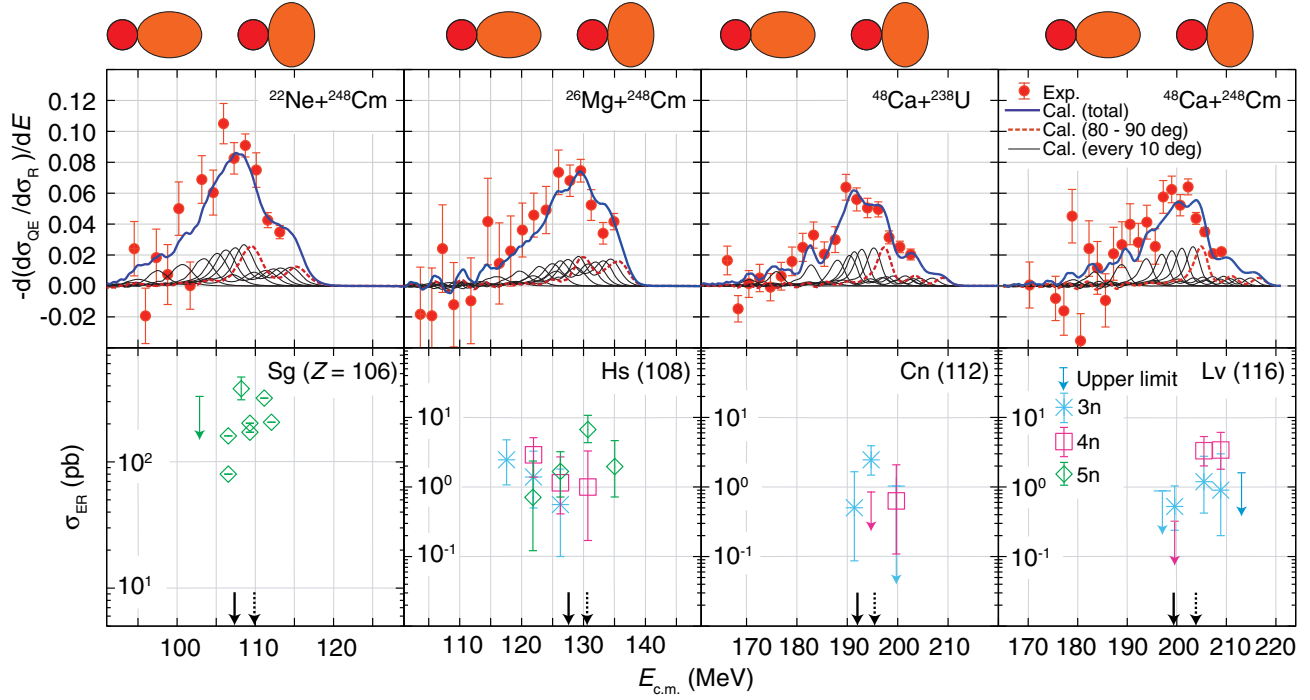


FIG. 3. A comparison between the measured QE barrier distributions (upper) and the evaporation residue cross sections reported at different center-of-mass energies for the syntheses of Sg, Hs, Cn, and Lv [8,47–54] (lower). The meanings of the red symbols and the blue solid curves are the same as in Fig. 2. The red dashed lines show the barrier distribution for the 80°–90° orientation angle of the target nuclei with respect to the beam direction. The black thin lines show the barrier distribution for every 10°, such as 0°–10°, 10°–20°, ..., 70°–80°. The solid and the dashed black arrows denote the average Coulomb barrier height B_0 , corresponding to the energy point at which $d\sigma_{QE}/d\sigma_R$ is 0.5 and the Coulomb barrier height of the side collision B_{side} , respectively.

the reaction of $^{22}\text{Ne} + ^{248}\text{Cm}$, 0.25 for $^{26}\text{Mg} + ^{248}\text{Cm}$ and $^{48}\text{Ca} + ^{238}\text{U}$, and 0.24 for $^{48}\text{Ca} + ^{248}\text{Cm}$ were employed. The calculated results are shown in Figs. 2 and 3 by the solid blue lines. The experimental data are well reproduced by these calculations, indicating that the barrier distributions are significantly altered by excitations of the projectile nuclei and the neutron transfer, even though the deformation of the target nuclei provides a major contribution.

The experimental excitation functions for the ER cross sections [8,47–54] are shown in the bottom panels of Fig. 3. The solid and the dashed arrows indicate the experimentally determined average Coulomb barrier height B_0 , defined by $d\sigma_{QE}/d\sigma_R (E_{c.m.} = B_0) = 0.5$, and the Coulomb barrier height of the side collision B_{side} , respectively. Here, B_{side} was determined as follows. In the coupled-channels calculations, CCFULL employs a deformed Woods-Saxon potential, which leads to orientation-angle-dependent barrier heights $B(\theta)$ [34]. One can then define the (theoretical) average barrier height as

$$\bar{B} = \frac{\int_0^\pi B(\theta) \sin(\theta) d\theta}{\int_0^\pi \sin(\theta) d\theta}. \quad (1)$$

The same values for the parameters of r_0 , a_0 , r_w , a_w , V_w , β_2 , β_4 , and β_6 as those in the CCFULL calculations were used to

calculate the B_{side} . The s -wave scattering was assumed, since our experimental method yields the experimental Coulomb barrier distribution for $l \sim 0$. The depth of the Woods-Saxon potential is adjusted so that the average barrier height \bar{B} coincides with the experimental average barrier height B_0 , which eventually defines B_{side} as $B_{side} = B(90^\circ)$. Note that the above (below) barrier region corresponds to the side (tip) collision, which corresponds to the higher (lower) energy side in the top panels in Fig. 3 when the deformation of the target is taken into account.

By comparing (i) the peak of the sum of the ER cross sections, (ii) B_0 , and (iii) B_{side} , it is realized that the peaks of the ER cross sections appear above the B_0 and close to B_{side} , even though B_{side} may contain theoretical systematic errors due to uncertainties in the deformation parameters (e.g., B_{side} is altered from 109.9 to 111.9 MeV when β_4 and β_6 are switched off for the $^{22}\text{Ne} + ^{248}\text{Cm}$ reaction). Even if we had taken into account such uncertainties, the results clearly indicate that the evaporation residue cross sections are maximized for a compact collision. Considering that the survival probability decreases with the incident energy, the probability of compound nucleus (CN) formation should be large enough to yield the maximum of the ER cross sections at the side-collision energy. This could be associated with the compact configuration at the side collision in the touching phase between the colliding two nuclei.

Shorter charge-center distance at the contact between the nuclei would result in larger probability of CN formation, as discussed in Refs. [25,28,60,61].

Contribution from each colliding angle to the barrier distribution is systematically shown in Fig. 3 (black thin solid curves) by showing the barrier distribution from each colliding-angle range with a 10° interval. Here, the distribution for the side collision 80° – 90° is highlighted by the red dashed curve. The total barrier distributions, which are the sum of the black thin solid curves and the red dashed curves, are also shown by the blue solid curves. Notice that the Coulomb barrier distributions for every 10° are widened due to the other couplings, such as the inelastic excitations of the projectile nuclei and the neutron transfer channel. Of course, the peak of the sum of the ER cross sections coincides not only with the barrier distribution for 80° – 90° , but also with that for 70° – 80° , etc. However, the overlap with the barrier distribution for the tip collision, such as 0° – 20° , is negligibly small, indicating that these hot fusion reactions take advantage of the compact collision.

A comparison between the total barrier distribution and the individual barrier distributions for every 10° implies that the effect of the target deformation is stronger in widening the barrier distribution as compared to that of the other couplings, even though the latter also contributes significantly. Evidently, several coupling effects, including the deformation and the inelastic excitations in the colliding nuclei, should be taken into account in theoretical calculations to understand the reaction mechanism for synthesizing SHN with hot fusion reactions.

In conclusion, the excitation functions of quasielastic scattering cross sections for reactions relevant to the syntheses of SHN, that is, the $^{22}\text{Ne} + ^{248}\text{Cm}$, $^{26}\text{Mg} + ^{248}\text{Cm}$, and $^{48}\text{Ca} + ^{238}\text{U}$ systems, were measured to understand the reaction dynamics of the hot fusion reactions. The experimental data were well reproduced by the coupled-channels calculations, which demonstrates the importance of the deformation of the target nuclei. From a comparison between the experimentally determined barrier distribution and the ER cross sections for Sg, Hs, Cn, and Lv, the ER cross sections peak at an energy in between the average Coulomb barrier height and that for the side collision. Moreover, it was also found that the peaks coincide with the Coulomb barrier distribution for compact collisions, such as 70° – 90° . This suggests that the evaporation residue cross sections are enhanced at energies that correspond to a compact collision where the projectile approaches along the short axis of a prolately deformed nucleus.

We point out that the optimum incident energy for the hot fusion reaction can be estimated by an experimentally determined barrier distribution as indicated in this Letter, if the trend of compact collision is not changed. Importantly, it would take only about one day to measure a barrier distribution for one reaction, which is much shorter than a typical experiment to synthesize new SHE, e.g., more than

100 days using one μA beam (6.2×10^{12} particle/s). This new method will significantly contribute to future experiments to synthesis both new SHE and SHN in the island of stability. Another important fact is that this determination is almost independent of theoretical predictions, which may include a large model dependence.

The experiments of this study were performed at the RI Beam Factory operated by RIKEN Nishina Center and Center for Nuclear Study (CNS), University of Tokyo. We would like to thank the accelerator staffs for their excellent operation and assistance during the experiments. In particular, we are grateful to Dr. M. Kidera for providing stable beams and RILAC accelerator operators for managing several fast energy changes during the night and day. ^{248}Cm material was provided by the U.S. DOE Isotope Program. This research was partially supported by a Grant-in-Aid for Specially Promoted Research, 19002005, from the Ministry of Education, Culture, Sports, Science and Technology of Japan, and by the U.S. DOE Office of Nuclear Physics. T. T. thanks the RIKEN Junior Research Associate Program.

-
- [1] A. Sobiczewski, F. A. Gareev, and B. N. Kalinkin, *Phys. Lett.* **22**, 500 (1966).
 - [2] W. D. Myers and W. J. Swiatecki, *Nucl. Phys.* **81**, 1 (1966).
 - [3] U. Mosel and W. Greiner, *Z. Phys.* **222**, 261 (1969).
 - [4] M. Bender, K. Rutz, P. G. Reinhard, J. A. Maruhn, and W. Greiner, *Phys. Rev. C* **60**, 034304 (1999).
 - [5] H. Koura, *Prog. Theor. Exp. Phys.* **2014**, 113D02 (2014).
 - [6] Y. T. Oganessian, V. K. Utyonkov, Y. V. Lobanov, F. S. Abdullin, A. N. Polyakov *et al.*, *Phys. Rev. C* **69**, 021601(R) (2004).
 - [7] Y. T. Oganessian, V. K. Utyonkov, Y. V. Lobanov, F. S. Abdullin, A. N. Polyakov *et al.*, *Phys. Rev. C* **69**, 054607 (2004).
 - [8] Y. T. Oganessian, V. K. Utyonkov, Y. V. Lobanov, F. S. Abdullin, A. N. Polyakov *et al.*, *Phys. Rev. C* **70**, 064609 (2004).
 - [9] Y. T. Oganessian, V. K. Utyonkov, Y. V. Lobanov, F. S. Abdullin, A. N. Polyakov *et al.*, *Phys. Rev. C* **74**, 044602 (2006).
 - [10] Y. T. Oganessian, F. S. Abdullin, P. D. Bailey, D. E. Benker, M. E. Bennett *et al.*, *Phys. Rev. Lett.* **104**, 142502 (2010).
 - [11] C. E. Düllmann, *EPJ Web Conf.* **131**, 08004 (2016).
 - [12] S. Hofmann *et al.*, *Eur. Phys. J. A* **52**, 180 (2016).
 - [13] S. Dmitriev, M. Itkis, and Y. Oganessian, *EPJ Web Conf.* **131**, 08001 (2016).
 - [14] C. E. Düllmann, *EPJ Web Conf.* **163**, 00015 (2017).
 - [15] T. Tanaka and K. Morita, *AAPPS Bull.* **28**, No. 3, 28 (2018).
 - [16] V. I. Zagrebaev and W. Greiner, *Phys. Rev. C* **78**, 034610 (2008).
 - [17] L. Zhu, W. J. Xie, and F. S. Zhang, *Phys. Rev. C* **89**, 024615 (2014).
 - [18] N. Ghahramanya and A. Ansari, *Eur. Phys. J. A* **52**, 287 (2016).

- [19] G. G. Adamian, N. V. Antonenko, and H. Lenske, *Nucl. Phys.* **A970**, 22 (2018).
- [20] K. Hagino, *Phys. Rev. C* **98**, 014607 (2018).
- [21] Y. Aritomo *et al.*, *J. Phys. Soc. Jpn. Conf. Proc.* **23**, 013001 (2018).
- [22] K. Sekizawa and K. Hagino, *Phys. Rev. C* **99**, 051602(R) (2019).
- [23] S. S. Ntshangase *et al.*, *Phys. Lett. B* **651**, 27 (2007).
- [24] S. Mitsuoka, H. Ikezoe, K. Nishio, K. Tsuruta, S. C. Jeong, and Y. Watanabe, *Phys. Rev. Lett.* **99**, 182701 (2007).
- [25] T. Tanaka *et al.*, *J. Phys. Soc. Jpn.* **87**, 014201 (2018).
- [26] M. Dasgupta *et al.*, *Annu. Rev. Nucl. Sci.* **48**, 401 (1998).
- [27] B. B. Back, H. Esbensen, C. L. Jiang, and K. E. Rehm, *Rev. Mod. Phys.* **86**, 317 (2014).
- [28] D. J. Hinde, M. Dasgupta, J. R. Leigh, J. P. Lestone, J. C. Mein, C. R. Morton, J. O. Newton, and H. Timmers, *Phys. Rev. Lett.* **74**, 1295 (1995).
- [29] E. M. Kozulin *et al.*, *Phys. Rev. C* **96**, 064621 (2017).
- [30] A. B. Balantekin and N. Takigawa, *Rev. Mod. Phys.* **70**, 77 (1998).
- [31] N. Rowley, G. R. Satchler, and P. H. Stelson, *Phys. Lett. B* **254**, 25 (1991).
- [32] H. Timmers, J. R. Leigh, M. Dasgupta, D. J. Hinde, R. C. Lemmon, J. C. Mein, C. R. Morton, J. O. Newton, and N. Rowley, *Nucl. Phys.* **A584**, 190 (1995).
- [33] J. R. Leigh *et al.*, *Phys. Rev. C* **52**, 3151 (1995).
- [34] K. Hagino and N. Takigawa, *Prog. Theor. Phys.* **128**, 1061 (2012).
- [35] G. G. Adamian, N. V. Antonenko, and W. Scheid, *Nucl. Phys.* **A678**, 24 (2000).
- [36] D. J. Hinde, M. Dasgupta, and A. Mukherjee, *Phys. Rev. Lett.* **89**, 282701 (2002).
- [37] K. Morita *et al.*, *Nucl. Instrum. Methods Phys. Res., Sect. B* **70**, 220 (1992).
- [38] K. Morita *et al.*, *Eur. Phys. J. A* **21**, 257 (2004).
- [39] K. Hagino and N. Rowley, *Phys. Rev. C* **69**, 054610 (2004).
- [40] F. L. H. Wolfs, W. Henning, K. E. Rehm, and J. P. Schiffer, *Phys. Lett. B* **196**, 113 (1987).
- [41] T. Nakagawa, Y. Higurashi, M. Kidera, T. Aihara, M. Kase, and Y. Yano, *Nucl. Instrum. Methods Phys. Res., Sect. B* **226**, 392 (2004).
- [42] M. Odera *et al.*, *Nucl. Instrum. Methods Phys. Res.* **227**, 187 (1984).
- [43] K. Ozeki, T. Kageyama, M. Kidera, Y. Higurashi, and T. Nakagawa, *Rev. Sci. Instrum.* **86**, 016114 (2015).
- [44] Y. Kudou, H. Haba, K. Ooe, D. Kaji, K. Morimoto, A. Shinohara, and K. Morita, *RIKEN Accel. Prog. Rep.* **42**, 265 (2009).
- [45] See Supplemental Material at <http://link.aps.org/supplemental/10.1103/PhysRevLett.124.052502> for deriving the experimental values.
- [46] T. Tanaka, Doctoral dissertation, Kyushu University, 2019, https://catalog.lib.kyushu-u.ac.jp/opac_download_md/2236025/sci1328.pdf.
- [47] S. Hübener, S. Taut, A. Vahle, R. Dressler, B. Eichler, H. W. Gäggeler, D. T. Jost, D. Piguët, A. Türler, and W. Brüchle, *Radiochim. Acta* **89**, 737 (2001).
- [48] H. Haba, D. Kaji, Y. Kudou, K. Morimoto, K. Morita *et al.*, *Phys. Rev. C* **85**, 024611 (2012).
- [49] J. Dvorak, W. Bruchle, M. Chelnokov, C. E. Dullmann, Z. Dvorakova *et al.*, *Phys. Rev. Lett.* **100**, 132503 (2008).
- [50] S. Hofmann *et al.*, *Eur. Phys. J. A* **32**, 251 (2007).
- [51] S. Hofmann *et al.*, *Eur. Phys. J. A* **48**, 62 (2012).
- [52] Y. A. Lazarev, Y. V. Lobanov, Y. T. Oganessian, V. K. Utyonkov, F. S. Abdullin *et al.*, *Phys. Rev. Lett.* **73**, 624 (1994).
- [53] A. Türler, R. Dressler, B. Eichler, H. W. Gäggeler, D. T. Jost, M. Schädel, W. Brüchle, K. E. Gregorich, N. Trautmann, and S. Taut, *Phys. Rev. C* **57**, 1648 (1998).
- [54] R. Dressler, B. Eichler, D. T. Jost, A. Türler, R. Eichler, and H. W. Gäggeler, *PSI Rep.* **1**, 130 (1999).
- [55] K. Hagino, N. Rowley, and A. T. Kruppa, *Comput. Phys. Commun.* **123**, 143 (1999).
- [56] O. Akyüz and A. Winther, in *Proceedings of the International School of Physics "Enrico Fermi," Course LXXVII*, edited by R. A. Broglia, C. H. Dasso, and R. A. Ricci (North-Holland, Amsterdam, 1981), p. 492.
- [57] S. Raman, C. W. Nestor, Jr., and P. Tikkanen, *At. Data Nucl. Data Tables* **78**, 1 (2001).
- [58] P. Möller, A. J. Sierk, T. Ichikawa, and H. Sagawa, *At. Data Nucl. Data Tables* **109–110**, 1 (2016).
- [59] R. H. Spear, *At. Data Nucl. Data Tables* **42**, 55 (1989).
- [60] K. Nishio, H. Ikezoe, S. Mitsuoka, and J. Lu, *Phys. Rev. C* **62**, 014602 (2000).
- [61] E. Vardaci, M. G. Itkis, I. M. Itkis, G. Knyazheva, and E. M. Kozulin, *J. Phys. G* **46**, 103002 (2019).